





RESEARCH ARTICLE

Design and singularity analysis of a parallel mechanism with origami-inspired reconfigurable 5R closed-loop linkages

Yili Kuang^{1,2} , Haibo Qu^{1,2,3} , Xiao Li^{1,2} , Xiaolei Wang^{1,2}  and Sheng Guo^{1,2,3}

¹Robotics Research Center, School of Mechanical, Electronic and Control Engineering, Beijing Jiaotong University, Beijing, China

²Research Center of Robotics Technology and Equipment, Tangshan Research Institute, Beijing Jiaotong University, Tangshan, China

³Key Laboratory of Vehicle Advanced Manufacturing, Measuring and Control Technology, Ministry of Education, Beijing Jiaotong University, Beijing, China

Corresponding author: Haibo Qu; Email: hbqu@bjtu.edu.cn

Received: 15 July 2023; **Revised:** 22 March 2024; **Accepted:** 27 March 2024; **First published online:** 19 April 2024

Keywords: single-vertex origami; reconfigurable parallel mechanism; configuration change; variable workspace; singularity analysis

Abstract

The reconfigurable mechanisms can satisfy the requirements of changing environments, working conditions, and tasks on the function and performance of the mechanism and can be applied to machine tool manufacturing, space detection, etc. Inspired by the single-vertex fivefold origami pattern, a new reconfigurable parallel mechanism is proposed in this paper, which has special singular positions and stable motion due to replicating the stabilizing kinematic properties of origami. Through analyzing the topologic change of the folding process of the pattern and treating it as a reconfigurable joint, a new reconfigurable parallel mechanism with 3, 4, 5, or 6 degrees of freedom is obtained. Then, the kinematics solution, workspace, and singularity of the mechanism are calculated. The results indicate that the singular configuration of the origami-derived reconfigurable parallel mechanism is mainly located in a special plane, and the scope of the workspace is still large after the configuration change. The mechanism has the potential to adapt to multiple tasks and working conditions through the conversion among different configurations by folding reconfigurable joints on the branch chain.

Nomenclature

$\alpha_{i(i+1)}$:	crease angle.
φ_i :	dihedral angle.
$c\theta$:	cosine of θ .
$s\theta$:	sine of θ .
e_i :	unit vector.
\hat{S}_r :	constraint screw.
J_x :	constraint Jacobian.
J_q :	actuation Jacobian.
r_1 :	radius of the fixed base.
r_2 :	radius of the moving platform.
d_i :	actuation parameters of prismatic pair P.
ψ :	angle of the passive spherical hinge.
R_{eqv1} :	state 1 of the spherical 5R mechanism.

$R_{\text{eqv}2}$:	state 2 of the spherical 5R mechanism.
ϕ_i :	rotation angle of $R_{\text{eqv}1}$.
θ_i :	rotation angle of $R_{\text{eqv}2}$.
$\$$:	screw in plücker coordinate.
\vec{s}_i :	direction vector of the axis of the kinematic pair.
jR_i :	rotation matrix from coordinate i to coordinate j .
$\$p$:	instantaneous motion screw of the moving platform.
q :	input of the reconfigurable parallel mechanism

1. Introduction

The reconfigurable mechanisms can satisfy the requirements of changing environments, working conditions, and tasks on the function and performance of the mechanism and can be applied to machine tool manufacturing [1], space detection [2–3], etc. Moreover, the *reconfigurable parallel mechanism* (RPM) is concerned due to its advantages of large bearing capacity and high precision [4]. At present, the reconfigurable parallel mechanism is mainly designed as follows: reconfigurable joints [5–13], reconfigurable kinematic chain [14–20], reconfigurable moving platform [21–24], reconfigurable fixed base [25], etc. Through conferring the moving platforms, bases, joints, branched chains, and other components with variable motions or topologies, a reconfigurable generalized parallel mechanism can be constructed.

In addition to the existing literatures on reconfigurable moving platforms and bases, numerous studies have focused on reconfigurable joints and branch reconfigurable problems caused by the singularity of the single loop branch chain. Various reconfigurable joints have been designed, such as reconfigurable Hooke joint with the orientation of connector T changeable (rT) [5], reconfigurable revolute joint (rR) [8], and reconfigurable spherical variable-axis joint (Sv) [9], proposed various new reconfigurable mechanisms and evaluated their performance [12–13]. Hu et al. [6] synthesized a kind of actuating reconfigurable parallel spherical joint, which is capable of realizing one-dimensional fixed-axis rotation and one-dimensional variable-axis rotation, two-dimensional and three-dimensional rotation. Li et al [7] proposed a reconfigurable axial joint inspired by Rubik's Cubes, which evolved from two types of spherical joints to three types of variable hook joints and one type of revolute joint.

The research on reconfigurable kinematic chains is mainly realized by the bifurcation characteristics of limbs. Ye et al. [14–15] designed a multi-rhombic metamorphic limb with multiple motion branches and constructed a kind of planar reconfigurable parallel mechanism. Wei et al. investigated a novel RPM based on the bifurcation of planar subgroup SE (2) and rotational subgroup SO (3) in the transformed configuration space [19] and studied the configuration switching and path selection of the novel RPM based on the subgroup SE (2), SO (3) and X (z) [20].

Some studies have proposed a series of reconfigurable mechanisms by regarding special origami structures as reconfigurable joints or reconfigurable limbs [26–31]. Dai [26–27] proposed the reconfigurable mechanism with variable topology and variable freedom in the research on the gift box packaging. Fang [28] designed a new type of parallel mechanism with three degrees of freedom (DOFs) based on the origami structure, whose moving platform and the base center are always coaxial under special geometric constraints. Wang [29] suggested an 8R reconfigurable quadruped mobile robot based on an origami structure. Inspired by a kirigami structure, Zhang [30] designed a novel reconfigurable parallel mechanism. Through the method of graph theory and group theory enumeration, Barreto [31] derived a kind of multi-circuit spherical parallel mechanism based on the origami design theorem.

To sum up, reconfigurable branches and joints are mainly realized by variable topology structures, whose characteristics and selection depend on researchers' own experience. Hence, origami is one of the inspiration sources for constructing RPM in many studies due to its relevancy with variable topology structure. Based on the box folding pattern with a single vertex and fivefold [32], a spherical reconfigurable closed-loop chain is designed and its motion characteristics are studied in this paper. Then, a novel RPM is proposed, and its various kinematic performances are analyzed, which provides ideas for the

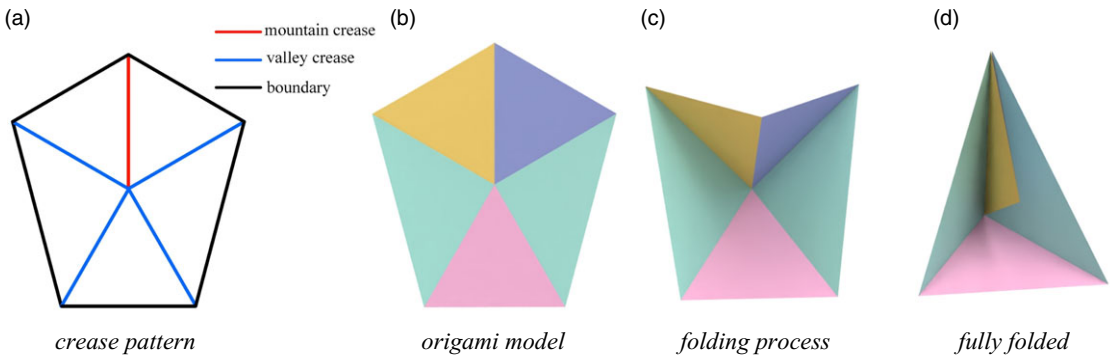


Figure 1. The box fold pattern with a single vertex and five creases and its folding process.

design and analysis of reconfigurable parallel mechanisms. The arrangement of this paper is as follows: section 2 analyzes the spherical reconfigurable linkages inspired by a single-vertex fivefold origami pattern, and puts forward a new RPM based on its motion characteristics and configuration switching by folding. Section 3 analyzes the variation of motion performance of the reconfigurable parallel mechanism, including its inverse kinematics, workspace, and singularity. Eventually, the innovations and perspectives of this study are summarized in section 4.

2. Spherical 5R closed-loop linkage and its derived reconfigurable mechanism

2.1. Reconfigurable spherical closed-loop chain inspired by origami

Origami is an art form that transforms two-dimensional paper into a three-dimensional structure based on predesigned crease patterns. Origami structures are widely used in the engineering field due to their advantages, such as being foldable, deformable, and motion stable [33–34]. During the folding process, the paper surface is regarded as a link rotating around the creases, and the paper that does not deform except for the creases is called rigid origami. The geometric elements of origami are composed of vertices and creases. According to the number of creases per single vertex, the origami structure can be divided into fourfold structures (such as Miura-ora units), fivefold structures, sixfold structures (such as Diamond units and Kresling units [35–36]), eightfold structures, etc.

Since single-vertex fourfold origami conventionally only has a single degree of freedom [37] and does not have topological changes; while single-vertex sixfold origami has three rotational DOF [38], if it is regarded as a reconfigurable closed-chain joint with topology changes by locking certain joints, its variable motion analysis will relatively more complicated than fivefold origami pattern. This article designs a spherical reconfigurable motion joint based on a box fold pattern with a single vertex with fivefold. A single-vertex fivefold pattern, as shown in Fig. 1, is commonly used in the design of paper box folding [32]. In Fig. 1, the red line represents a mountain crease, the blue line represents a valley crease, and the black line represents the boundary.

Fig. 2 shows the geometric parameters and equivalent folding mechanism of the single vertex fivefold pattern. Given the parameters $\alpha_{23} = \alpha_{51} = \pi/2$, $\alpha_{34} = \alpha_{45} = \alpha$, and $\alpha_{12} = \pi - 2\alpha$, the motion of this origami pattern is equivalent to a spherical 5R mechanism [39], as shown in Fig. 2(b). Under a spherical coordinate system, the foldable mechanism’s displacement can be expressed as two moving DOFs on a sphere centered in the vertex of five creases.

The motion characteristics and singularity of a single-vertex fivefold pattern in its folding process are analyzed as follows. First, the unit direction vectors of revolute pairs’ axis can be written as $\vec{s}_1 = [0 \quad -\sin(\alpha_{12}/2) \quad \cos(\alpha_{12}/2)]^T$, $\vec{s}_2 = [0 \quad \sin(\alpha_{12}/2) \quad \cos(\alpha_{12}/2)]^T$, $\vec{s}_3 = [a_3 \quad b_3 \quad c_3]^T$, $\vec{s}_4 = [a_4 \quad b_4 \quad c_4]^T$, $\vec{s}_5 = [a_5 \quad b_5 \quad c_5]^T$. Using the paper surface 1 as a fixed base and assuming that the direction

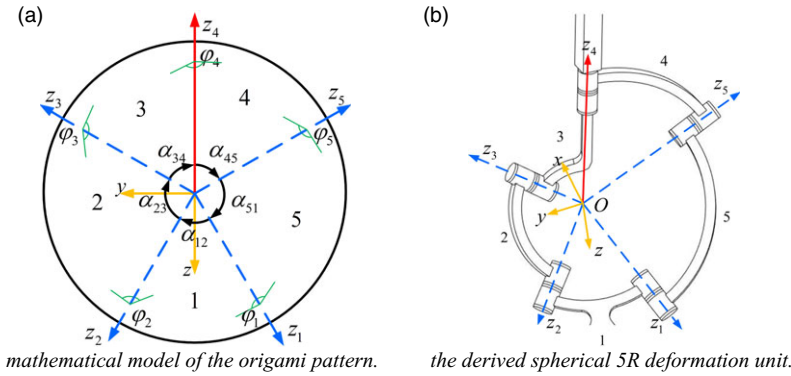


Figure 2. Single-vertex fivefold origami pattern and its derived spherical 5R deformation mechanism.

vector \vec{s}_4 of the crease between the paper surface 3 and the paper surface 4 is a known value, then calculating the positions of the remaining crease axes according to geometric constraints as follows.

Since $\vec{s}_2 \cdot \vec{s}_3 = 0$ and $\vec{s}_1 \cdot \vec{s}_5 = 0$, it can be solved separately: $c_3 = -b_3 \cot \alpha$, $c_5 = b_5 \cot \alpha$. Based on screw theory and structural parameters $\alpha_{i(i+1)}$, and regarding link 1 as the fixed base and link 4 as the output link, the kinematic screw of two branch chains can be expressed as Eq. (1).

$$\mathcal{S}_A = \begin{cases} \mathcal{S}_2 = [0 \ \cos \alpha \ \sin \alpha; 0 \ 0 \ 0]^T \\ \mathcal{S}_3 = [a_3 \ b_3 \ -b_3 \ \cot \alpha; 0 \ 0 \ 0]^T \\ \mathcal{S}_4 = [a_4 \ b_4 \ c_4; 0 \ 0 \ 0]^T \end{cases}, \quad \mathcal{S}_B = \begin{cases} \mathcal{S}_1 = [0 \ -\cos \alpha \ \sin \alpha; 0 \ 0 \ 0]^T \\ \mathcal{S}_5 = [a_5 \ b_5 \ b_5 \ \cot \alpha; 0 \ 0 \ 0]^T \end{cases} \quad (1)$$

Since $\alpha_{34} = \alpha_{45} = \alpha$, Eq. (2) can be obtained.

$$\vec{s}_3 \cdot \vec{s}_4 = \cos \alpha, \quad \vec{s}_4 \cdot \vec{s}_5 = \cos \alpha \quad (2)$$

From Eq. (2), $a_3 = (\cos \alpha - b_3(b_4 - c_4 \cot \alpha))/a_4$ and $a_5 = (\cos \alpha - b_5(b_4 + c_4 \cot \alpha))/a_4$ can be obtained. According to $a_3^2 + b_3^2 + (-b_3 \cot \alpha)^2 = 1$ and $a_5^2 + b_5^2 + (b_5 \cot \alpha)^2 = 1$, b_3 and b_5 can be solved with each has two sets of solutions. Depending on the direction in which the crease is folded, one set of solutions can be eliminated and a unique solution can be obtained, as follows:

$$b_3 = \frac{\cos \alpha (b_4 - c_4 \cot \alpha) + \sqrt{a_4^2 (a_4^2 (1 + \cot^2 \alpha) - \cot^2 \alpha + (b_4 - c_4 \cot \alpha)^2)}}{a_4^2 (1 + \cot^2 \alpha) + (b_4 - c_4 \cot \alpha)^2} \quad (3)$$

$$b_5 = \frac{\cos \alpha (b_4 + c_4 \cot \alpha) - \sqrt{a_4^2 (a_4^2 (1 + \cot^2 \alpha) - \cot^2 \alpha + (b_4 + c_4 \cot \alpha)^2)}}{a_4^2 (1 + \cot^2 \alpha) + (b_4 + c_4 \cot \alpha)^2}$$

Solving the reciprocal screw of two limbs' screw systems \mathcal{S}_A and \mathcal{S}_B , and obtaining the kinematic screw of output link 4, which can be expressed as Eq. (4).

$${}^0\mathcal{S} = \begin{cases} {}^0\mathcal{S}_1 = [a \ 0 \ 1; 0 \ 0 \ 0]^T \\ {}^0\mathcal{S}_2 = [b \ 1 \ 0; 0 \ 0 \ 0]^T \end{cases} \quad (4)$$

where $a = -\frac{\cot \alpha (b_4 b_5 - \cos \alpha + b_5 c_4 \cot \alpha)}{a_4 b_5 (1 + \cot^2 \alpha)}$, $b = -\frac{b_4 b_5 - \cos \alpha + b_5 c_4 \cot \alpha}{a_4 b_5 (1 + \cot^2 \alpha)}$.

As shown in Fig. 2(a), $\varphi_i (i = 2, 3, \dots, 5)$ shows the dihedral angle formed by the paper surface i and $i - 1$, φ_1 especially presents the dihedral angle formed by the paper surface 5 and paper surface 1. The rotation angle corresponding to φ_i is denoted as θ_i . The mountain crease surrounded by paper surface 3 and paper surface 4 has a dihedral angle $\varphi_4 \in [0, \pi]$ and an auxiliary rotation angle $\theta_4 = \varphi_4 - \pi, \in [-\pi, 0]$. According to the folding process of the origami pattern shown in Fig. 1, link 3 and link 4 will

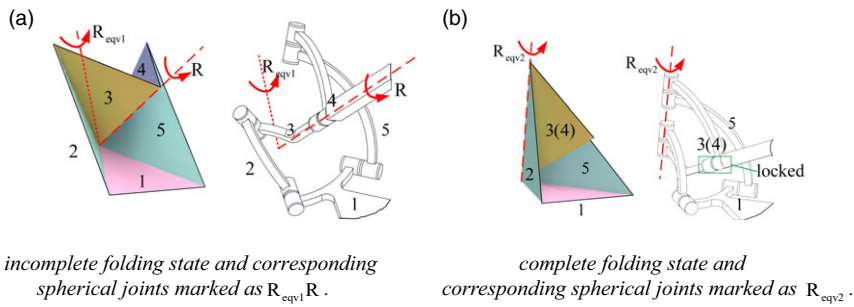


Figure 3. Topological changes of the spherical deformation 5R joints before and after folding.

be regarded as cemented together and treated as a single link, denoted as link 3(4), when the actuator φ_4 is locked at the fully folded state. The branch screw system $\$A$ becomes:

$$\$A = \begin{cases} \$2 = [0 \ \cos \alpha \ \sin \alpha; 0 \ 0 \ 0]^T \\ \$3 = [a_3 \ b_3 \ -b_3 \ \cot \alpha; 0 \ 0 \ 0]^T \end{cases} \tag{5}$$

the kinematic screw of the output link 3(4) becomes:

$${}^0\$ = [c \ d \ 1; 0 \ 0 \ 0]^T \tag{6}$$

where $c = \frac{2 \sin^2 \alpha (\cos \alpha - b_3 (b_4 - c_4 \cot \alpha)) (\cos \alpha - b_5 (b_4 + c_4 \cot \alpha))}{a_4 (2b_3 b_5 c_4 + \sin \alpha (b_5 - b_3))}$, $d = \frac{\cos \alpha (b_3 + b_5) - 2b_3 b_4 b_5 \cot \alpha}{2b_3 b_5 c_4 \cot \alpha + \cos \alpha (b_5 - b_3)}$.

So, the output motion of link 3(4) is reduced to one rotational DOF on the axis $[c \ d \ 1]^T$. Especially, when the dihedral angle $\varphi_4 = 0$ is locked, which means $\vec{s}_3 = \vec{s}_5 = [1 \ 0 \ 0]^T$, the kinematic screw of the spherical mechanism becomes:

$${}^0\$ = [1 \ 0 \ 0; 0 \ 0 \ 0]^T \tag{7}$$

Eq. (7) represents the rotation around the x-axis, which is consistent with the DOF after fully folding the dihedral angle φ_4 of origami.

The geometric topology and motion characteristics of the spherical mechanism have changed corresponding to the singular configuration of the origami. The equivalent joint that corresponds to the state of incomplete folding of origami is defined as $R_{eqv1} R$ with two rotational DOFs; when the origami is fully folded, the spherical 5R joint becomes a single rotational motion record as R_{eqv2} , as shown in Fig. 3 (a) and (b), respectively.

The spherical 5R mechanism is regarded as a reconfigurable joint, and its two reconfigurable forms are $R_{eqv1} R$ and R_{eqv2} , which correspond to the topological states of incomplete folding and complete folding of origami, respectively. When the reconfigurable joint is $R_{eqv1} R$, the two rotations of output link 4: the screw expression of the equivalent rotation pair R_{eqv1} is shown in Eq. (6); And R is a rotating pair composed of link 3 and link 4. When the reconfigurable joint is R_{eqv2} , the motion screw of output link 3(4) is written as Eq. (7).

2.2. Derived reconfigurable parallel mechanism

Based on the spherical unit shown in Fig. 3, a triangular box fold pattern can be formed, whose crease pattern and folding process are shown in Fig. 4.

The single-vertex fivefold origami is equivalent to the spherical 5R mechanism shown in Fig. 3. Using this spherical mechanism as a special kinematic pair and combining it into the form of Fig. 4, a reconfigurable parallel mechanism is designed, as shown in Fig. 5. The initial installation state of the spherical 5R mechanism is consistent with the distribution of mountain and valley creases in the fivefold origami, so its movement process is equivalent to the folding process of origami. Based on the stability of the unidirectional motion of origami, the different solutions of the closed-loop kinematic chain are

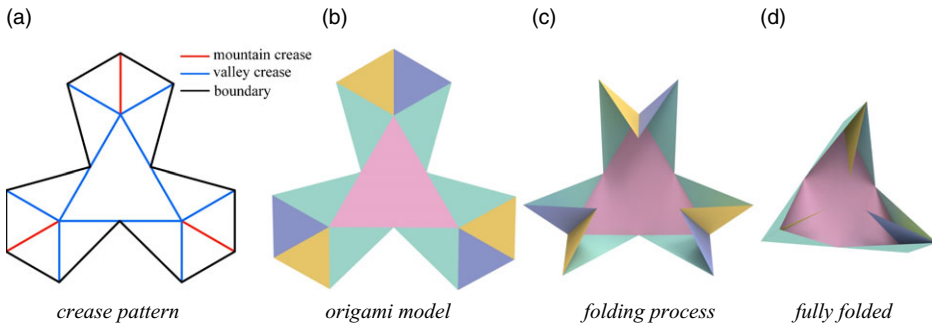


Figure 4. Triangle box fold pattern and its folding process.

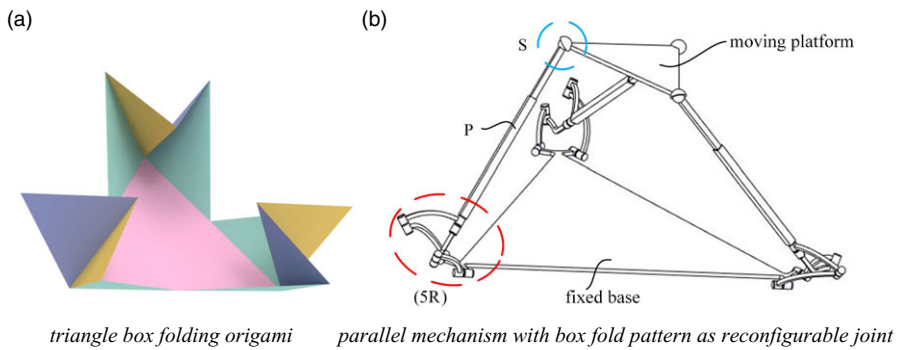


Figure 5. Origami-inspired 3 – (5R)PS reconfigurable parallel mechanism.

avoided, which is conducive to reducing the complexity of kinematic analysis of spatially closed-loop mechanisms by replicating the unidirectional actuation of creases. The spherical 5R joint can realize stable driving of the reconfigurable parallel mechanism.

Each branch chain includes a spherical 5R joint, a prismatic pair (P), and a spherical hinge (S). The 3 – (5R)PS reconfigurable parallel mechanism has four configurations with 6, 5, 4, or 3 DOFs, respectively, as shown in Fig. 6. s_{i1} and s_{i2} represent the rotating axis direction of the reconfigurable 5R joint, and s_{i3} represents the axis direction of the moving pair in the i th branch chain. Based on the reciprocity between the constraint force and the kinematic screw [40], it can be seen that the branch chain including a reconfigurable joint R_{eqv1} has no constraint on the moving platform, while the branch chain including a reconfigurable joint R_{eqv2} provides a restraint force F_i against the moving platform, with the direction of F_i perpendicular to s_{i3} that the axis of prismatic pair and coplanar with s_{i1} that the axis direction of the reconfigurable joint R_{eqv2} .

3. Kinematic analysis of different configurations

Kinematics and singularity analysis are important mathematical methods for evaluating the performance of parallel mechanisms [41–42] and have made contributions to helping researchers improve mechanism performance and promote the practical application of new mechanisms. Soheil [43] presented a systematic method to obtain singular configurations of spherical mechanisms with input and output links. Gallant and Gosselin [44] proposed a method of singularity robust balancing for parallel manipulators passing through type II singular configurations, which characteristically arise within the workspace while following inconsistent trajectories. In this paper, vector equations are used to analyze the inverse kinematic solutions of four different configurations of the 3 – (5R)PS reconfigurable parallel

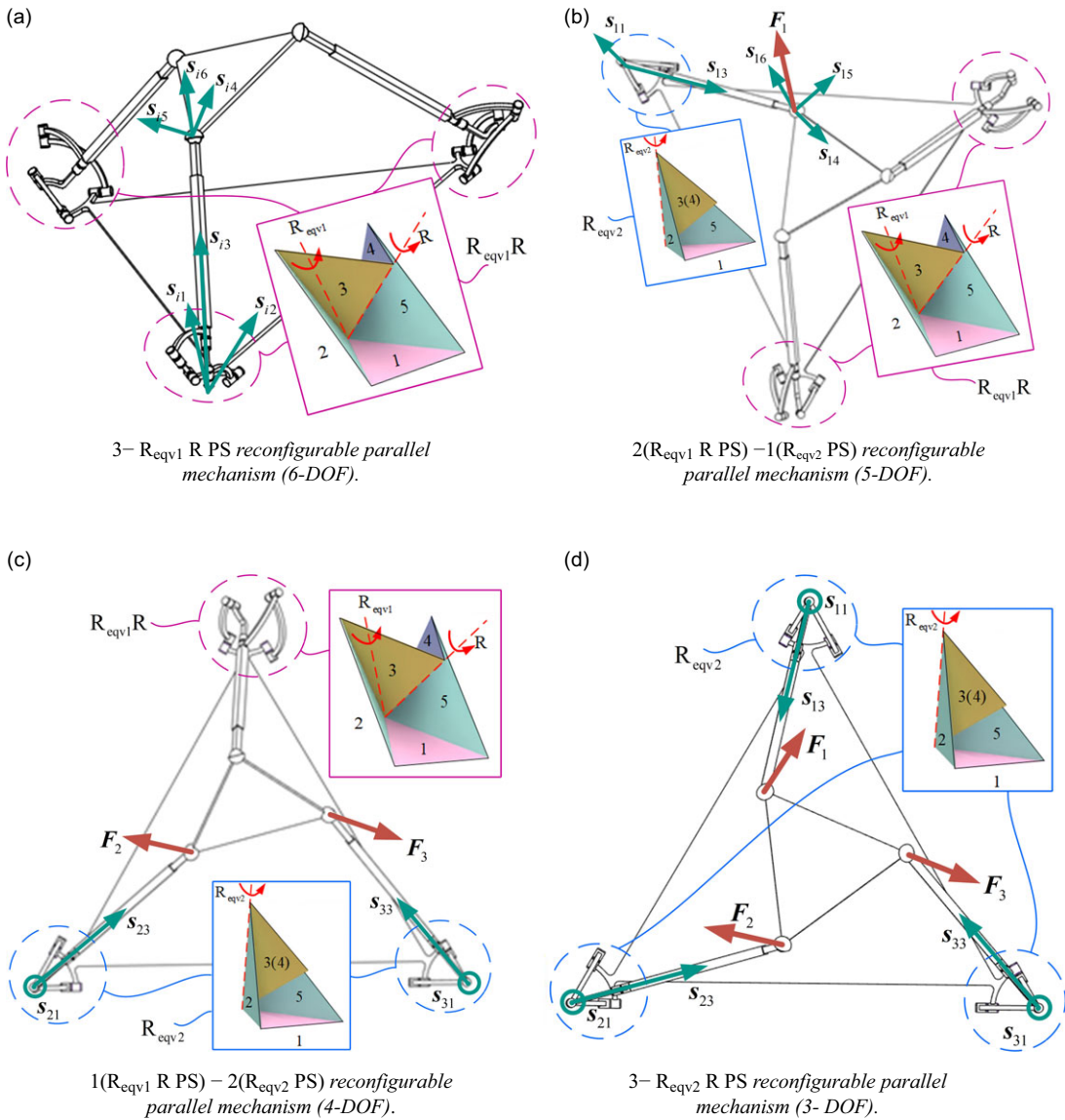


Figure 6. Four different configurations of 3 – (5R)PS reconfigurable parallel mechanisms.

mechanism. The Jacobian matrix of different configurations are derived through the screw reciprocity product, and the singularities of the RPM in different configurations are analyzed based on the numerical algorithm.

3.1. Inverse kinematic solutions

Fig. 7 established the moving platform coordinate system $P - uvw$ and the branch chain coordinate system $A_i - x_{Ai}y_{Ai}z_{Ai} (i = 1, 2, 3)$. $OA_i = r_1$ and $PB_i = r_2$ are, respectively, the circumcircle radius of fixed base and movable platform, and d_i is the length of prismatic pair. If the pose $P(x, y, z), \theta_x, \theta_y$ and θ_z of the moving platform is known, the actuation parameters $d_1, d_2, d_3, \theta_{41}, \theta_{42},$ and θ_{43} can be inversely solved as follows.

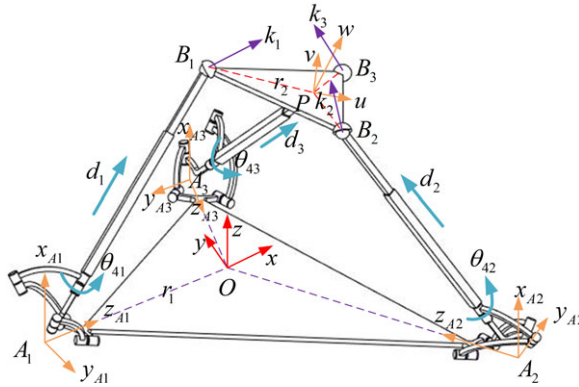


Figure 7. Inverse kinematics: 3 – (5R)PSreconfigurable parallel mechanism.

In the basic coordinate system $O - xyz$, points A_1, A_2 , and A_3 can be expressed as

$$A_1 = [-r_1 \ 0 \ 0]^T, A_2 = \left[\frac{r_1}{2} \quad -\frac{\sqrt{3}r_1}{2} \quad 0 \right]^T, A_3 = \left[\frac{r_1}{2} \quad \frac{\sqrt{3}r_1}{2} \quad 0 \right]^T \tag{8}$$

In the moving platform coordinate system $P - uvw$, point B_1, B_2 , and B_3 can be expressed as

$${}^pB_1 = [-r_2 \ 0 \ 0]^T, {}^pB_2 = \left[\frac{r_2}{2} \quad -\frac{\sqrt{3}r_2}{2} \quad 0 \right]^T, {}^pB_3 = \left[\frac{r_2}{2} \quad \frac{\sqrt{3}r_2}{2} \quad 0 \right]^T \tag{9}$$

In the basic coordinate system $O - xyz$, point B_1, B_2 , and B_3 can be expressed as

$$B_1 = {}^0R_p {}^pB_1 + P, B_2 = {}^0R_p {}^pB_2 + P, B_3 = {}^0R_p {}^pB_3 + P \tag{10}$$

where ${}^0R_p = Rz(\theta_z)Ry(\theta_y)Rx(\theta_x)$ represents the rotational transformation matrix from the moving coordinate system $P - uvw$ to the base coordinate system $O - xyz$.

Therefore, the vector $\vec{A_iB_i} (i = 1, 2, 3)$ in the base coordinate system $O - xyz$ is

$$\vec{A_iB_i} = B_i - A_i = [l_i, m_i, n_i]^T, i = 1, 2, 3 \tag{11}$$

where the formulae for l_i, m_i, n_i are given in the Appendix.

Then the actuator d_i of the prismatic pair can be obtained,

$$d_i = \sqrt{l_i^2 + m_i^2 + n_i^2}, i = 1, 2, 3 \tag{12}$$

The transformation matrix from the branch coordinate system $A_i - x_{A_i}y_{A_i}z_{A_i} (i = 1, 2, 3)$ to the base coordinate system $O - xyz$ can be written as

$${}^0R_{A1} = Rz(\pi) Ry(-\pi/2), {}^0R_{A2} = {}^0R_{A1}Rx(2\pi/3), {}^0R_{A3} = {}^0R_{A1}Rx(-2\pi/3) \tag{13}$$

The unit vector $\vec{A_iB_i}$ can be expressed at coordinate system $O - xyz$:

$${}^0e_i = A_iB_i/|A_iB_i| = [x_i, y_i, z_i]^T, (i = 1, 2, 3) \tag{14}$$

In the branch chain coordinate system, $A_i - x_{A_i}y_{A_i}z_{A_i} (i = 1, 2, 3)$, \vec{s}_{4i} represents the direction vector of the revolute joint θ_{4i} :

$$\vec{s}_{4i} = [a_{4i}, b_{4i}, c_{4i}]^T, i = 1, 2, 3 \tag{15}$$

Eq. (15) can be transformed to the base coordinate system:

$${}^0e_i = {}^0R_{A_i} \vec{s}_{4i}, i = 1, 2, 3 \tag{16}$$

\vec{s}_{4i} is calculated from Eq. (16), then substitute into Eq. (2) to find two sets of solutions for \vec{s}_{3i} and \vec{s}_{5i} . Due to the characteristics of valley creases, one set of solutions can be omitted to obtain a unique solution. The dihedral angle φ_{4i} can be obtained by calculating quantity product between the unit normal vectors of paper surface 3 and paper surface 4, as the formula: $\cos(\pi - \varphi_{4i}) = (\vec{s}_{3i} \times \vec{s}_{4i} / \sin \alpha) \cdot (\vec{s}_{4i} \times \vec{s}_{5i} / \sin \alpha)$, and then the actuation angle $\theta_{4i} = \varphi_{4i} - \pi, (i = 1, 2, 3)$ can be obtained.

Without loss of generality, when locking the revolute pair actuator θ_{4i} of the i th branch chain, A_iB_i is represented in the branch chain coordinate system:

$$A_iB_i = d_i (\cos \alpha, \sin \alpha \sin \phi_i, \sin \alpha \cos \phi_i)^T \tag{17}$$

As shown in Eq. (17), ϕ_i is the angle between the projection of the vector A_iB_i on the plane $y_{Ai}A_i z_{Ai}$ and the axis y_{Ai} . A_iB_i can be represented in the base coordinate system by left-multiplying the rotation matrix ${}^0R_{Ai}$.

There have been divided into three situations when reconfigurable joints are locked.

1. When locking $\theta_{41} = -\pi$, the first branch chain becomes a $R_{\text{eqv2}}PS$ branch chain, which provides a constraint force through the center of the spherical joint for the moving platform. The moving platform has 5 DOF, whose dependent pose parameter z can be represented by independent parameters x, y, θ_x, θ_y , and θ_z . From Eq. (11) and Eq. (17), it can be found that

$$d_1 \cos \alpha = z + r_2 \sin \theta_y \tag{18}$$

By subtracting the squares of Eq. (12) and Eq. (18), the driving d_1 can be determined, and substituting it with Eq. (18) can determine the positional parameters z . According to Eq. (12) and Eq. (16), the actuators d_2, d_3, θ_{42} , and θ_{43} are solved.

2. When locking the two prismatic pairs' actuators, the moving platform has 4 DOF. Yet the general to simplify the analysis, locking the actuators that θ_{42} and θ_{43} , and the dependent pose parameters of the moving platform are taken as x and y . Calculating d_2 and d_3 as Eq. (19).

$$\begin{cases} d_2 \cos \alpha = z - r_2 (\sqrt{3}c\theta_y s\theta_x + s\theta_y) / 2 \\ d_3 \cos \alpha = z + r_2 (\sqrt{3}c\theta_y s\theta_x - s\theta_y) / 2 \end{cases} \tag{19}$$

Substituting Eq. (19) into Eq. (12) by subtracting the squares obtain that $y = (c_1 - b_1x)/a_1$, where a, b , and c are expressions about z, θ_x, θ_y , and θ_z . Substituting y into Eq.(12) to find out x by excluding a set of bad solutions to obtain the representation of dependent pose parameters x and y concerning independent parameters z, θ_x, θ_y , and θ_z . Thereby, the inverse kinematic solution of the mechanism can be solved.

3. When all three prismatic pairs' actuators are locked, the mechanism degenerates into a $3 - R_{\text{eqv2}}PS$ mechanism. Taking the platform independent pose parameters as z, θ_x , and θ_y , the actuators d_1, d_2 , and d_3 are solved by Eq. (18) and (19). Substituting d_1, d_2 , and d_3 into Eq. (17) and solving three equations: $|B_1B_2|^2 = 3r_2^2, |B_2B_3|^2 = 3r_2^2$ and $|B_1B_3|^2 = 3r_2^2, \phi_1, \phi_2$ and ϕ_3 can be calculated by Newton's iterative numerical solution according to Eq. (17) since their analytical solutions cannot be found. Then the coordinates of B_1, B_2 , and B_3 can be calculated. By introducing a reference point $B_4 = (B_2 + B_3)/2$ to determine the position coordinates of the moving platform that $P(x, y, z) = B_4 + (B_1 - B_4)/3$. Then calculating $\theta_z = \arctan \left(\frac{(y-m_1)/(r_2c\theta_y)}{(r_1+x-l_1)/(r_2c\theta_y)} \right)$ according to Eq. (11). Hence, x, y , and θ_z have been solved.

Table I. The range of given actuators and the constraints of passive joints.

RPM configurations	Constraints
3 – R _{eqv1} RPS	120mm ≤ d ₁ , d ₂ , d ₃ ≤ 210mm, −π ≤ θ ₄₁ , θ ₄₂ , θ ₄₃ ≤ 0, 0 ≤ ψ ₁ , ψ ₂ , ψ ₃ ≤ π/3
2(R _{eqv1} RPS) – 1(R _{eqv2} PS)	120mm ≤ d ₁ , d ₂ , d ₃ ≤ 210mm, −π ≤ θ ₄₂ , θ ₄₃ ≤ 0, −α/2 ≤ φ ₁ ≤ α/2, 0 ≤ ψ ₁ , ψ ₂ , ψ ₃ ≤ π/3
1(R _{eqv1} RPS) – 2(R _{eqv2} PS)	120mm ≤ d ₁ , d ₂ , d ₃ ≤ 210mm, −π ≤ θ ₄₁ ≤ 0, −α/2 ≤ φ ₁ , φ ₂ ≤ α/2, 0 ≤ ψ ₁ , ψ ₂ , ψ ₃ ≤ π/3
3 – R _{eqv2} PS	120mm ≤ d ₁ , d ₂ , d ₃ ≤ 210mm, −α/2 ≤ φ ₁ , φ ₂ , φ ₃ ≤ α/2, 0 ≤ ψ ₁ , ψ ₂ , ψ ₃ ≤ π/3

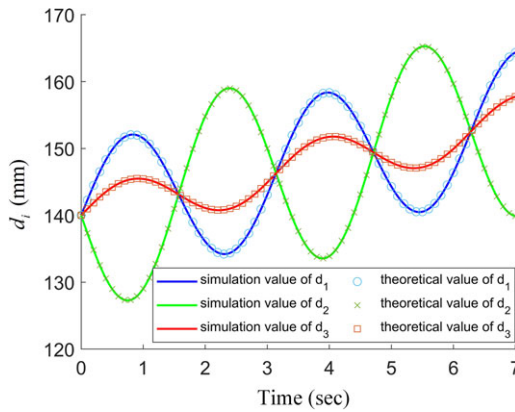


Figure 8. Verification of the kinematic inverse solution of the 3 – R_{eqv2}PS configuration with comparing simulation and theoretical values of the driving parameters.

Taking the 3 – R_{eqv2}PS configuration as an example, the mechanism motion simulation is performed after giving the initial position and motion trajectory of the moving platform. The simulation results are compared with the theoretical values calculated by the inverse solution to verify the correctness of the mechanism’s inverse kinematic solution. Setting the motion trajectory of the moving platform in the simulation software as shown in Eq. (20). As shown in Fig. 8, the simulated prismatic pair’s actuation parameter d_i is basically consistent with its theoretical calculation value, so the inverse solution calculation of the mechanism is believed to be correct and scientific.

$$\begin{cases} z = 70 + t \\ \theta_x = \pi \sin(2t) / 36 \\ \theta_y = \pi \sin(2t) / 36 \end{cases} \quad (20)$$

3.2. Workspace

Based on the inverse kinematic solution of the mechanism, the workspace of the reconfigurable parallel mechanism can be calculated using numerical methods. To prevent mutual interference between links, the range of given actuators and the constraints of passive joints are shown in Table I.

Note that $d_i(i = 1, 2, 3)$ refers to the prismatic actuator of the i th branch chain, with a range of 120mm ~ 210mm; $\theta_{4i}(i = 1, 2, 3)$ represents the actuator of the fourth rotation pair of the spherical 5R joint on the i th branch chain, whose range is $[-\pi, 0]$ consistent with the folding angle range of the origami; ϕ_i represents the rotation angle of the rotating pair R_{eqv2}, whose range is $[-\alpha/2, \alpha/2]$ when the i th branch chain’s spherical 5R linkage is equivalent to the R_{eqv2}; $\psi_i(i = 1, 2, 3)$ represents the rotation range of ball hinge on the i th branch chain. As shown in Fig. 7, here define ${}^P k_1 = [\sqrt{2}/2, 0, \sqrt{2}/2]^T$

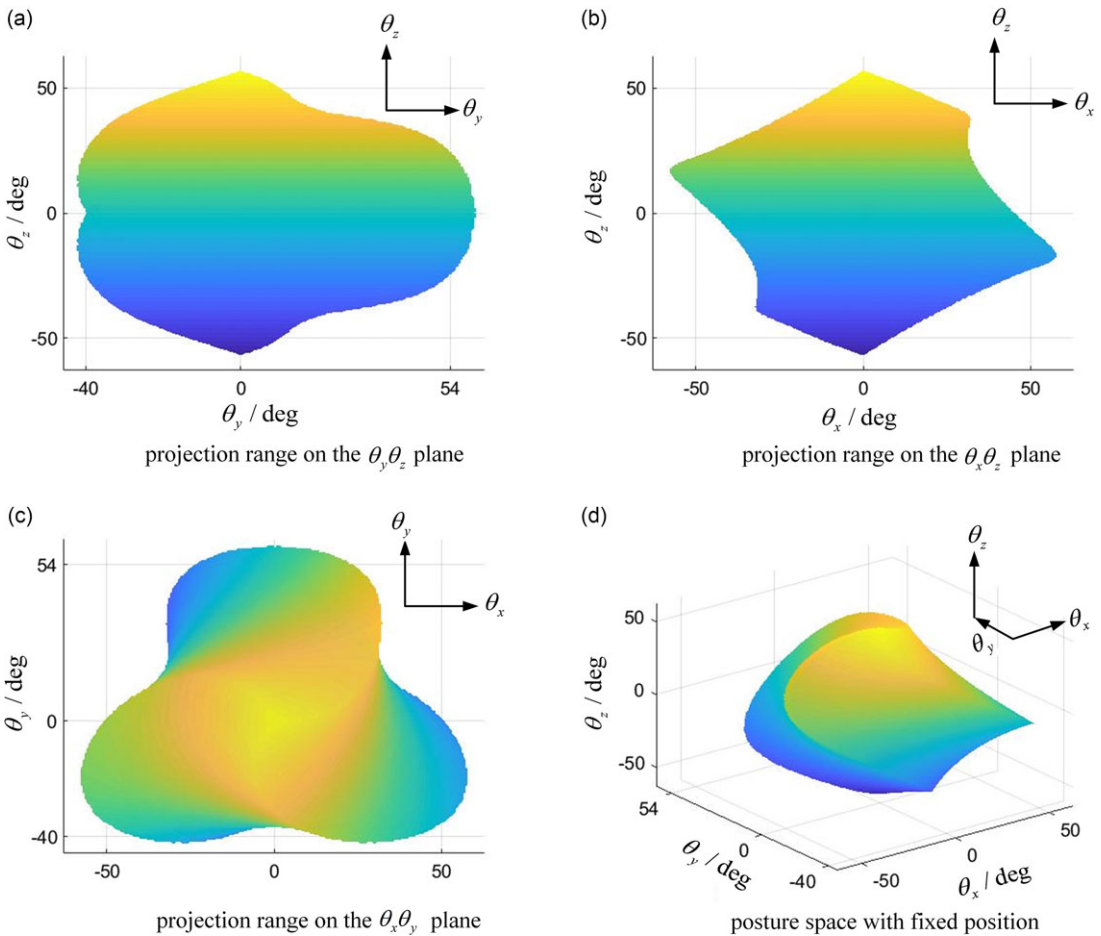


Figure 9. Posture space of 3 – R_{eqv1} RPS configuration when $x = y = 0\text{mm}$ and $z = 90\text{mm}$.

and express it as $k_1 = {}^0R_p \cdot {}^P k_1$ in the base coordinate system, so that $k_2 = {}^0R_p \cdot Rz(2\pi/3) \cdot {}^P k_1$ and $k_3 = {}^0R_p \cdot Rz(-2\pi/3) \cdot {}^P k_1$ can be obtained. The angle range of the passive spherical hinge of each branch chain can be expressed as ψ_i :

$$\psi_i = \arccos ({}^0e_i \cdot k_i), (i = 1, 2, 3) \tag{21}$$

Given the base size parameter $r_2 = 180\text{mm}$ and moving platform size parameter $r_1 = 60\text{mm}$, and taking the 3 – R_{eqv1} RPS configuration as an example, the workspace solution algorithm is shown in the Appendix Fig. A1.

Since the mechanism is in 3 – R_{eqv1} RPS configuration, the reachable pose space when the position fixes on $x, y = 0\text{mm}$ and $z = 90\text{mm}$ is shown in Fig. 9. In Fig. 9, (d) is the three-dimensional point cloud map of the moving platform reachable posture space, while (a), (b), and (c) are projection views of (d) in three basic planes. And by the same token, the workspaces of other reconfigurable configurations are shown in Figs. 10-14.

When the fixed posture is $\theta_x = \theta_y = \theta_z = 0$, the position space of the 3 – R_{eqv1} RPS configuration is shown in Fig. 10. It can be seen that the position space of the 3 – R_{eqv1} RPS configuration is symmetrically distributed along the y-axis.

When locking the revolute pair actuator $\theta_{41} = -\pi$ of the first branch chain, the position space is shown in Fig. 11 due to the posture parameter $\theta_x = \theta_y = \theta_z = 0$ being taken, and the posture space is shown in Fig. 12 as the position parameter $x = y = 0\text{mm}$ is taken.

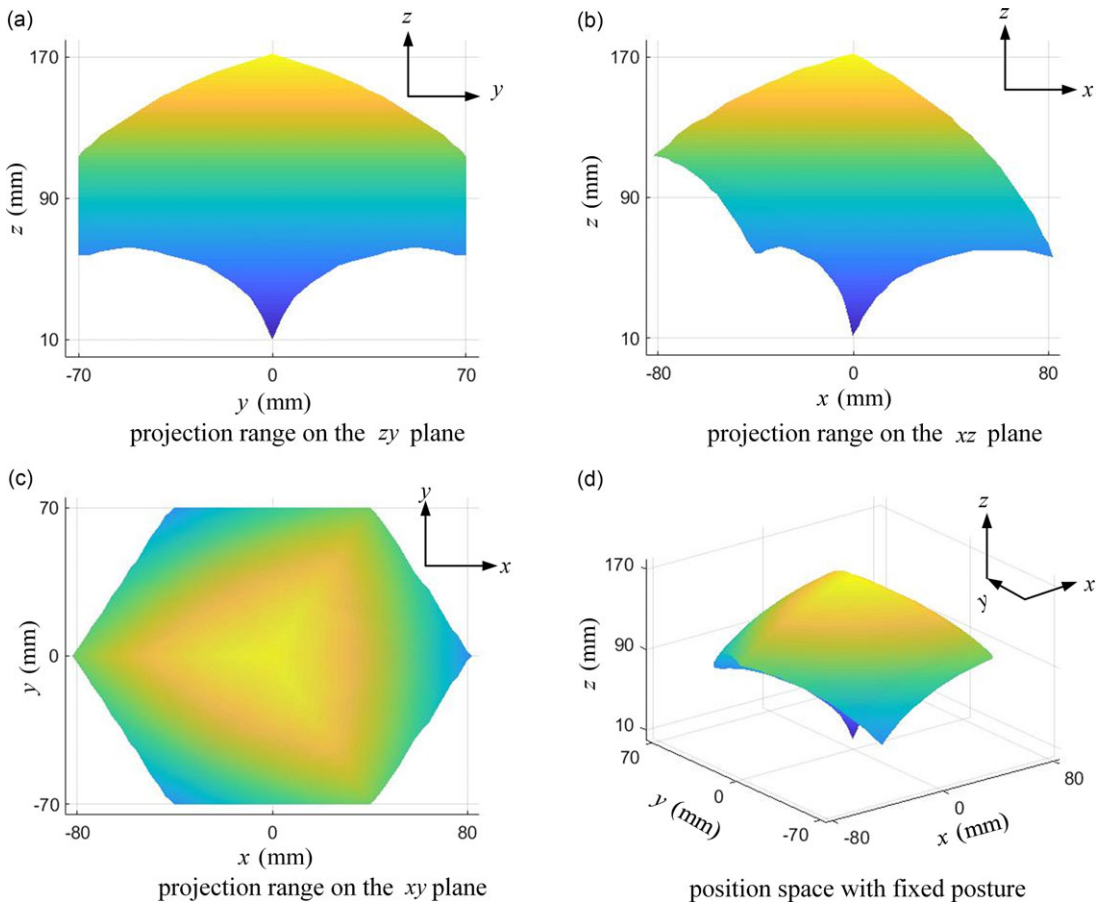


Figure 10. Position space of $3 - R_{eqv1}RPS$ configuration when $\theta_x = \theta_y = \theta_z = 0$.

The posture space of $2(R_{eqv1}RPS) - 1(R_{eqv1}PS)$ configuration with the fixed position shown in Fig. 12 is similar to the posture space of $3 - R_{eqv1}RPS$ configuration shown in Fig. 9. When locking the rotating pair actuator $\theta_{42} = \theta_{43} = -\pi$ of the second and third branch chains, the mechanism is $1(R_{eqv1}RPS) - 2(R_{eqv2}PS)$ configuration, which has 4-DOF. Suggesting the position parameter $z = 70\text{mm}$, its posture space is shown in Fig. 13. When locking the rotating pair actuator $\theta_{41} = \theta_{42} = \theta_{43} = -\pi$ of the first, second, and third branch chains, the mechanism becomes $3 - R_{eqv2}PS$ configuration, which has 3-DOF, and its workspace is shown in Fig. 14.

From Figs. 9 to 14, it can be seen that the working space of the mechanism has been reduced to a certain extent after locking the rotating pair actuator of the branch chain, but it can still achieve a large range of motion. So the new reconfigurable parallel mechanism proposed in this article has the potential for “one machine for multiple purposes”.

3.3. Singularity

The Jacobian matrix of the RPM is derived by using the concept of reciprocal screws, and the singularity positions of the mechanism are analyzed by calculating the determinant of the Jacobian matrix. Fig. 15 shows the kinematic screw on a single branch chain of the RPM when the spherical 5R joint is at two states of $R_{eqv1}R$ and R_{eqv2} . Where: the driving joint of the revolute pair of the branch chain can be represented as $\hat{\$}_{i2} = [a_i b_i^T A_i^T \times a_i b_i^T]^T$ in the base coordinate system; the equivalent rotational screw of the other four rotational joints of the spherical 5R joint can be denoted as

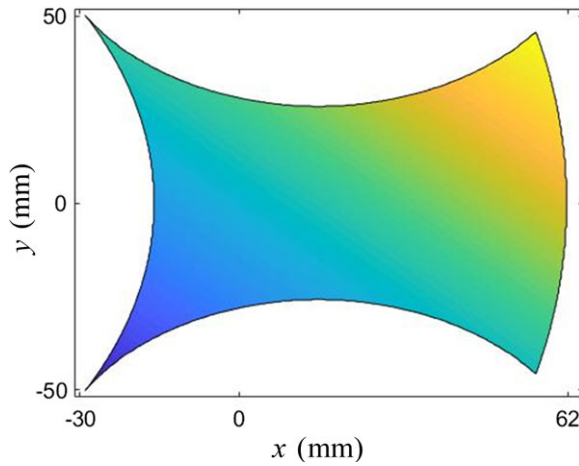


Figure 11. Position space of $2(R_{\text{eqv1}}\text{RPS}) - 1(R_{\text{eqv2}}\text{PS})$ configuration when $\theta_x = \theta_y = \theta_z = 0$.

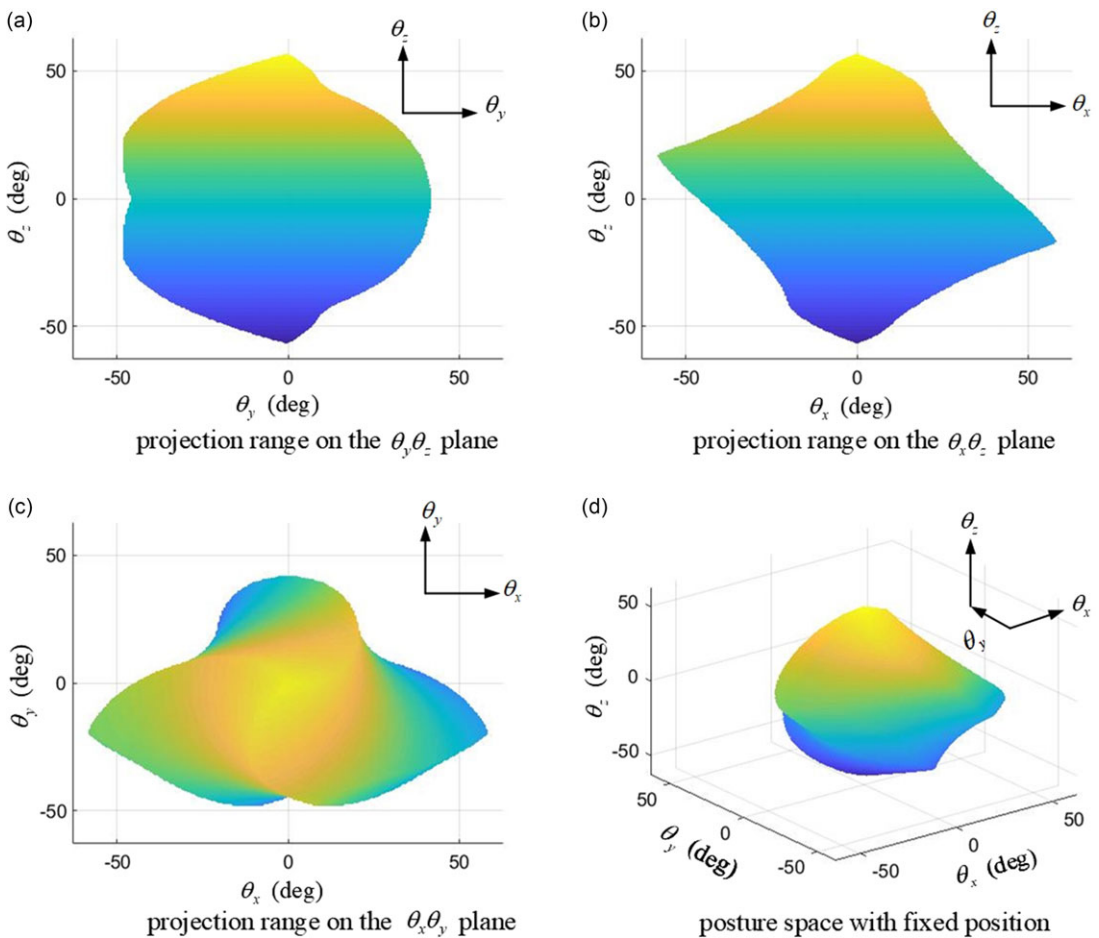


Figure 12. Posture space of $2(R_{\text{eqv1}}\text{RPS}) - 1(R_{\text{eqv2}}\text{PS})$ configuration when $x = y = 0\text{mm}$.

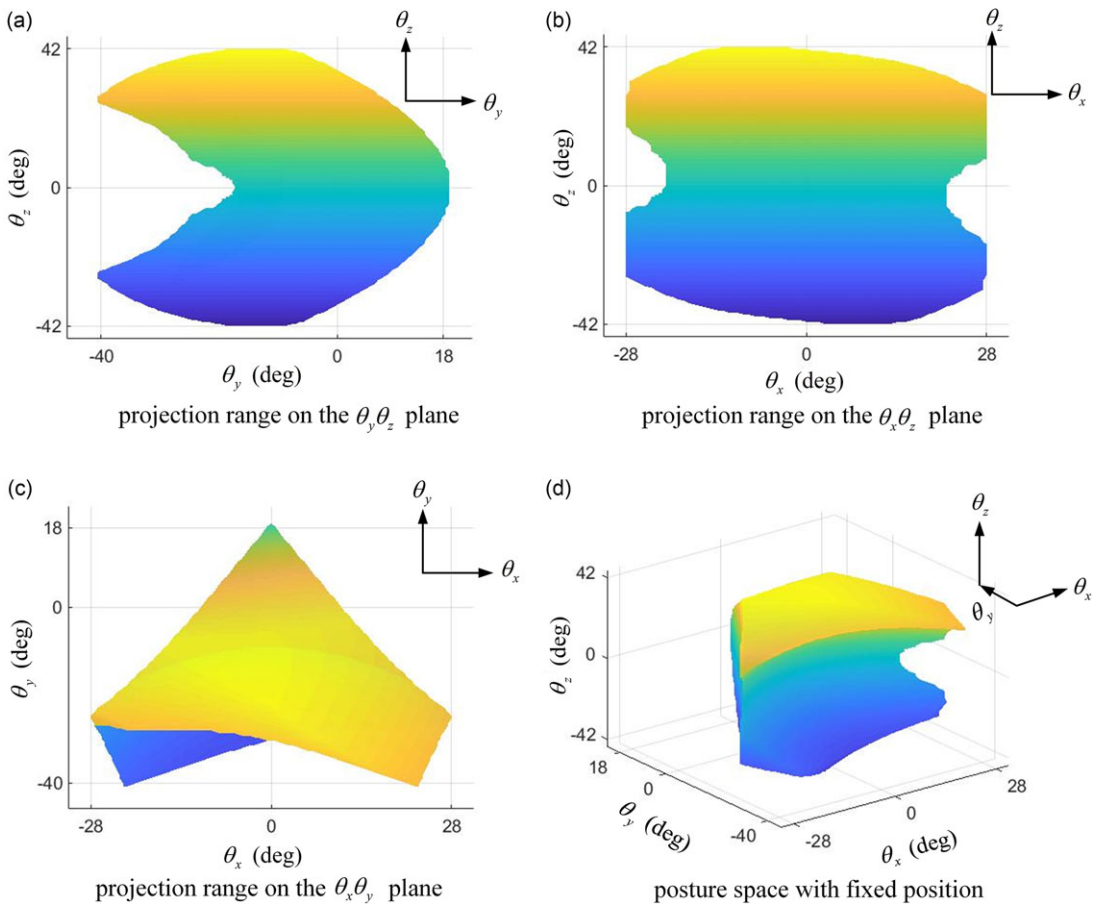


Figure 13. Posture space of 1(R_{eqv1} RPS) – 2(R_{eqv2} PS) configuration when $z = 70\text{mm}$.

$\hat{\$}_{i1} = [C_i^T A_i^T \times C_i^T]^T$, here $C_i = {}^0R_{A_i} \cdot [cd1]^T$ according to Eq. (6); the screw of the prismatic joint is recorded as $\hat{\$}_{i3} = [0^T a_i b_i^T]^T$; the ball hinge is decomposed into three mutually perpendicular rotating pair screws as $\hat{\$}_{i4} = [e_x^T B_i^T \times e_x^T]^T$, $\hat{\$}_{i5} = [e_y^T B_i^T \times e_y^T]^T$ and $\hat{\$}_{i6} = [e_z^T B_i^T \times e_z^T]^T$, here e_x, e_y and e_z represent the unit vector along the axis of x, y and z , respectively.

Considering each branch chain as an open chain, the instantaneous motion screw of the moving platform can be written as: $\$P = [\omega_n^T \quad v_0^T]^T$, which can be described as a linear combination of instantaneous motion spirals for each joint on the branch chain.

$$\$P = \dot{\theta}_1 \hat{\$}_{i1} + \dot{\theta}_2 \hat{\$}_{i2} + \dot{d}_i \hat{\$}_{i3} + \dot{\theta}_{i4} \hat{\$}_{i4} + \dot{\theta}_{i5} \hat{\$}_{i5} + \dot{\theta}_{i6} \hat{\$}_{i6} \quad (i = 1, 2, 3) \tag{22}$$

For a R_{eqv1} RPS branch chain, the two actuation screws are $\hat{\$}_{i2}$ and $\hat{\$}_{i3}$, and their constraint screws $\hat{\$}_{r1}$ and $\hat{\$}_{r2}$ can be calculated by being reciprocal to all other screws $\hat{\$}_{i1}, \hat{\$}_{i4}, \hat{\$}_{i5}, \hat{\$}_{i6}$ besides actuation screws. As shown in Eq. (23), note the product operations of the screws in this paper are all reciprocal product operations.

$$\hat{\$}_{r1}^T \$P = \hat{\$}_{r1}^T \hat{\$}_{i2} \dot{\theta}_2 + \hat{\$}_{r1}^T \hat{\$}_{i3} \dot{d}_i, \quad \hat{\$}_{r2}^T \$P = \hat{\$}_{r2}^T \hat{\$}_{i2} \dot{\theta}_2 + \hat{\$}_{r2}^T \hat{\$}_{i3} \dot{d}_i \tag{23}$$

However, due to the actuation screw $\hat{\$}_{i2}$ and the motion screws $\hat{\$}_{i4}, \hat{\$}_{i5}, \hat{\$}_{i6}$ of the ball joint always intersect at point B_i , $\hat{\$}_{r1}^T \hat{\$}_{i2} = 0$ is obtained.

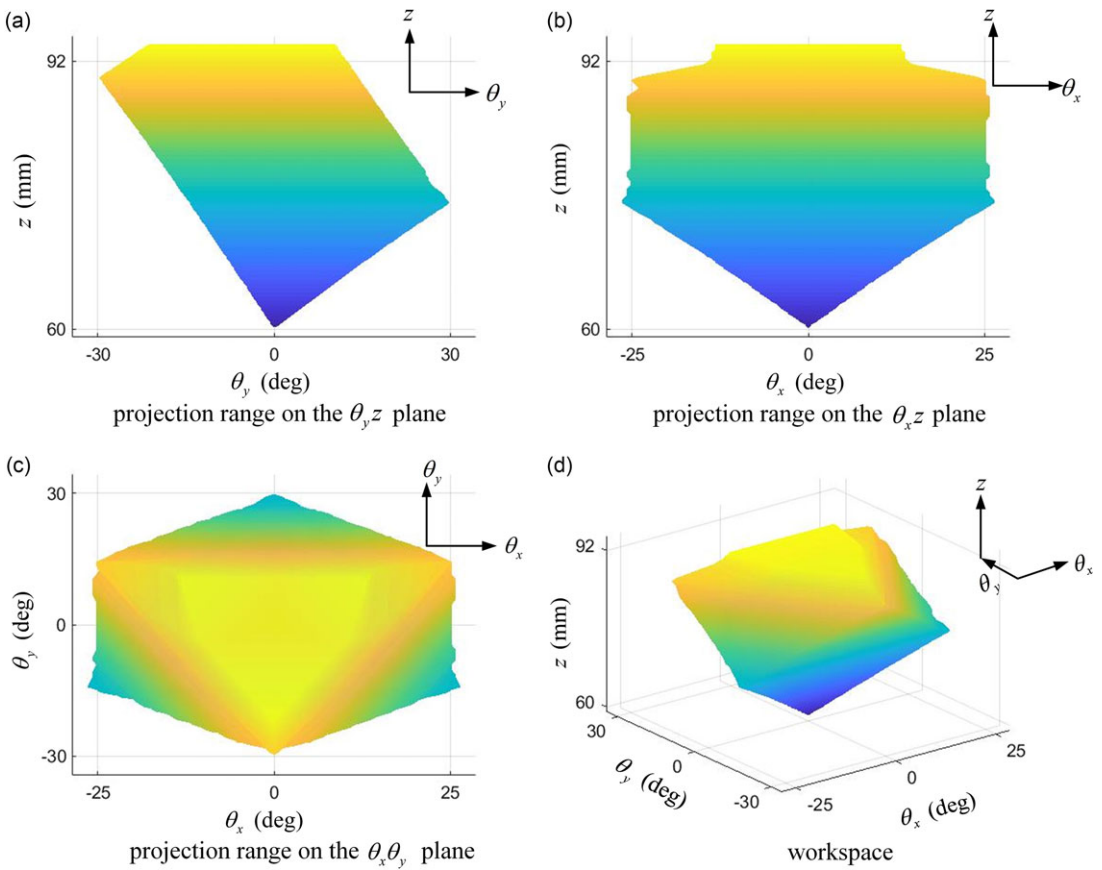


Figure 14. Workspace of 3 – R_{eqv2} PS configuration.

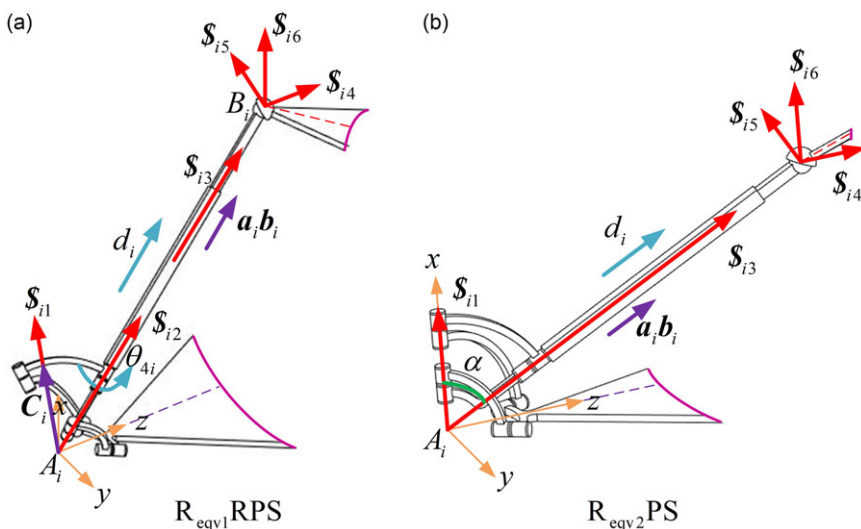


Figure 15. Motion screws of R_{eqv1} RPS and R_{eqv2} PS branch chains.

Table II. Values of constraint Jacobian matrix J_x and rotate joint actuator \dot{q}_i in different configurations of the RPM.

RPM configuration	$\hat{\$}_1^T$	$\hat{\$}_2^T$	$\hat{\$}_3^T$	$\hat{\$}_4^T$	$\hat{\$}_5^T$	$\hat{\$}_6^T$	\dot{q}_1	\dot{q}_2	\dot{q}_3
3 – R _{eqv1} RPS	$\hat{\$}_{r11}^T$	$\hat{\$}_{r12}^T$	$\hat{\$}_{r21}^T$	$\hat{\$}_{r22}^T$	$\hat{\$}_{r31}^T$	$\hat{\$}_{r32}^T$	$\dot{\theta}_{12}$	$\dot{\theta}_{22}$	$\dot{\theta}_{32}$
2(R _{eqv1} RPS) – 1(R _{eqv2} PS)	$\hat{\$}_{r1s}^T$	$\hat{\$}_{r13}^T$	$\hat{\$}_{r21}^T$	$\hat{\$}_{r22}^T$	$\hat{\$}_{r31}^T$	$\hat{\$}_{r32}^T$	0	$\dot{\theta}_{22}$	$\dot{\theta}_{32}$
1(R _{eqv1} RPS) – 2(R _{eqv2} PS)	$\hat{\$}_{r11}^T$	$\hat{\$}_{r12}^T$	$\hat{\$}_{r2s}^T$	$\hat{\$}_{r23}^T$	$\hat{\$}_{r3s}^T$	$\hat{\$}_{r33}^T$	$\dot{\theta}_{12}$	0	0
3 – R _{eqv2} PS	$\hat{\$}_{r1s}^T$	$\hat{\$}_{r13}^T$	$\hat{\$}_{r2s}^T$	$\hat{\$}_{r23}^T$	$\hat{\$}_{r3s}^T$	$\hat{\$}_{r33}^T$	0	0	0

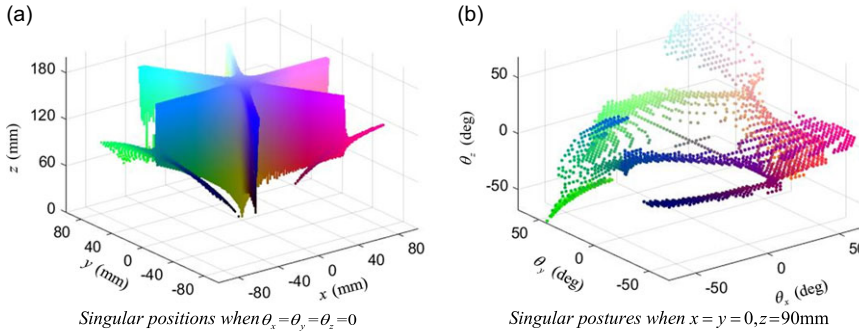


Figure 16. Singularity of 3 – R_{eqv1}RPS configuration.

For a R_{eqv2}PS branch chain, the actuation screw is $\hat{\$}_{i3}$ and the spherical 5R mechanism becomes a passive joint, whose motion screw $\hat{\$}_{i1}$ changes to $\hat{\$}_{i1} = [e_z^T A_i^T \times e_z^T]^T$. Since the R_{eqv2}PS branch chain has five DOFs, there is a constraint screw that is reciprocal to all screws on the branch chain:

$$\hat{\$}_{ris}^T \$_P = 0 \tag{24}$$

A screw that reciprocals to all but the actuation screw can be expressed as $\hat{\$}_{ri3} = [a_i b_i^T A_i^T \times a_i b_i^T]^T$, which satisfied the equation that $\hat{\$}_{ri3}^T \$_P = \hat{\$}_{ri3}^T \hat{\$}_{i3} \dot{d}_i$. Combining Eq. (22), Eq. (23), and Eq. (24) above can obtain the Jacobi of the mechanism $J_x \$_P = J_q \dot{q}_i$, which can be written as Eq. (25).

$$\begin{bmatrix} \hat{\$}_1^T \\ \hat{\$}_2^T \\ \hat{\$}_3^T \\ \hat{\$}_4^T \\ \hat{\$}_5^T \\ \hat{\$}_6^T \end{bmatrix} \$_P = \begin{bmatrix} Q_{11} & Q_{12} & 0 & 0 & 0 & 0 \\ Q_{21} & Q_{22} & 0 & 0 & 0 & 0 \\ 0 & 0 & Q_{33} & Q_{34} & 0 & 0 \\ 0 & 0 & Q_{43} & Q_{44} & 0 & 0 \\ 0 & 0 & 0 & 0 & Q_{55} & Q_{56} \\ 0 & 0 & 0 & 0 & Q_{65} & Q_{66} \end{bmatrix} \begin{bmatrix} \dot{q}_1 \\ \dot{d}_1 \\ \dot{q}_2 \\ \dot{d}_2 \\ \dot{q}_3 \\ \dot{d}_3 \end{bmatrix} \tag{25}$$

Here $J_x = \begin{bmatrix} \hat{\$}_1^T & \hat{\$}_2^T & \hat{\$}_3^T & \hat{\$}_4^T & \hat{\$}_5^T & \hat{\$}_6^T \end{bmatrix}^T$ is the constraint Jacobian matrix of the mechanism;

$J_q = \text{diag} \left(\begin{pmatrix} Q_{11} & Q_{12} \\ Q_{21} & Q_{22} \end{pmatrix}, \begin{pmatrix} Q_{33} & Q_{34} \\ Q_{43} & Q_{44} \end{pmatrix}, \begin{pmatrix} Q_{55} & Q_{56} \\ Q_{65} & Q_{66} \end{pmatrix} \right)$ is the actuation Jacobian matrix of the

mechanism; $\dot{q}_i = [\dot{q}_1 \ \dot{d}_1 \ \dot{q}_2 \ \dot{d}_2 \ \dot{q}_3 \ \dot{d}_3]^T$ is the input of the RPM.

For example, as to the 3 – R_{eqv1}RPS configuration, the constraint Jacobian and actuation Jacobian matrices are given by Eq. (18). The element values of the Jacobian matrix of different configurations are shown in Table II and Table AI.

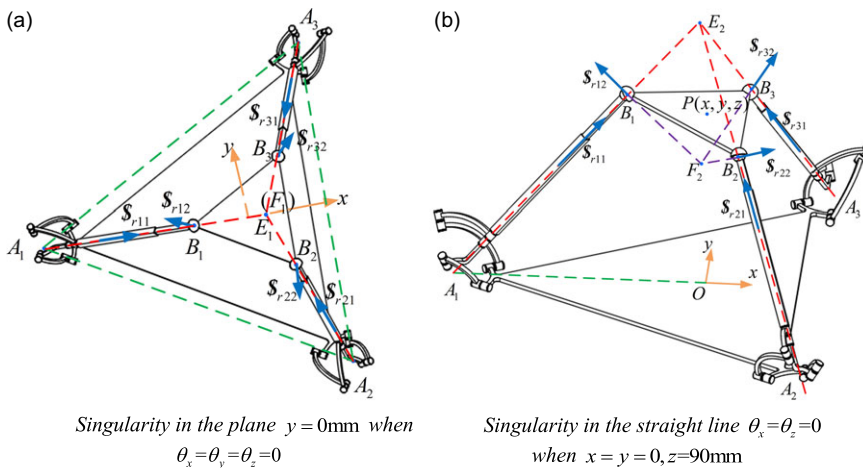


Figure 17. Verification diagram for singularity of 3 – R_{eqv1}RPS configuration.

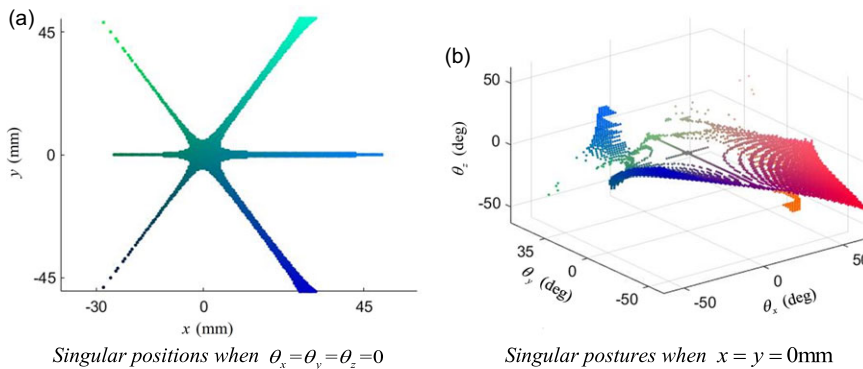


Figure 18. Singularity of 2(R_{eqv1}RPS) – 1(R_{eqv2}PS) configuration.

Taking the 3 – R_{eqv1}RPS configuration as an example, the numerical algorithm for solving the Jacobian matrix is shown in Fig. 16. The singularity of the constrained Jacobian matrix and determinant is solved by numerical method as shown in Appendix Fig. A2.

The special singular positions of the 3 – R_{eqv1}RPS configuration are singular planes as shown in Fig 16 (a), for example, the plane $y=0$. And its special singular postures are curved surfaces and special lines as shown in Fig. 16 (b), e.g. the intersection line of two planes: $\theta_z=0$ and $\theta_x=0$. Similarly, the singular configurations of the other three configurations can be obtained, as shown in Figs. 18-20.

Taking the 3 – R_{eqv1}RPS configuration as an example, the correctness of the singular configuration points obtained by the numerical solution was verified based on the line geometry method. The singularity verification diagram at the plane $y=0\text{mm}$ is shown in Fig. 18(a). When the posture of the moving platform is at $\theta_x=\theta_y=\theta_z=0$, the two actuation joints in each chain are locked and provided two constraint screw S_{r11} and S_{r12} for the moving platform, where S_{r11} is along the direction of prismatic pair, and S_{r12} passes through the center of the spherical hinge and is perpendicular to S_{r11} . When the position of the moving platform located in the plane of $y=0$, the constraint screw S_{r11} , S_{r21} , and S_{r31} are intersect at the point E_1 , and the constraint screw S_{r12} , S_{r22} , and S_{r32} are intersect at the point F_1 directly below the point E_1 . Therefore, the straight line E_1F_1 intersects the axes of six constraint screw at the same time, and the rank of the constraint screw system is 5. At this time, the degree of freedom of the moving platform increases while the mechanism behaves as constraint singularity. As branch chains of this mechanism are

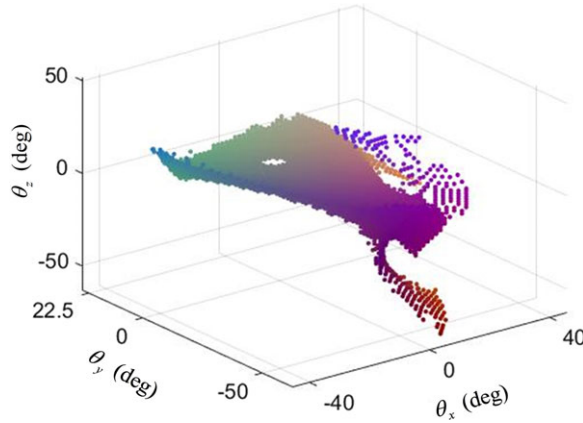


Figure 19. Singularity of $1(R_{eqv1}RPS) - 2(R_{eqv2}PS)$ configuration when $z = 70\text{mm}$.

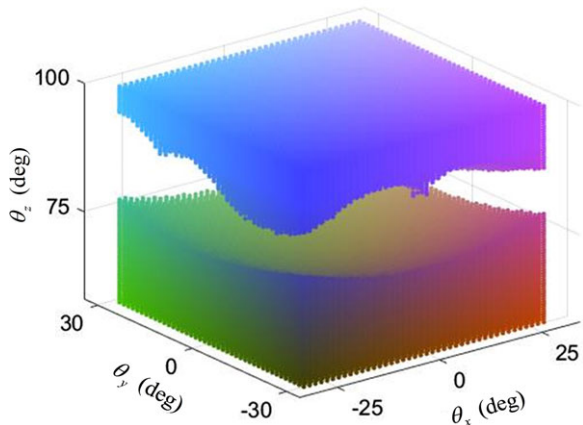


Figure 20. Singularity of $3 - R_{eqv2}PS$ configuration.

symmetrically distributed around the z -axis, we can draw the conclusion as shown in Fig. 17(a) that the singular points of this configuration are mainly distributed on three planes which intersect the z -axis. In the same way, as shown in Fig. 17(b), when the moving platform's position fixed at $x = y = 0, z = 90\text{mm}$, one of the singular straight lines in the $3 - R_{eqv1}RPS$ configuration is $\theta_x = \theta_z = 0$. The singularity verification diagram is shown in Fig. 18(b). It can be found that the straight line E_2F_2 intersects with all constraint screw, therefore, the mechanism is singularity with the rank of the constraint screw system of the moving platform is 5.

As shown in Fig 19(a), the singular positions of $2(R_{eqv1}RPS) - 1(R_{eqv2}PS)$ configuration are concentrated near the three straight lines passing through the origin, and its singular posture is mainly concentrated on singular planes $\theta_z = 0$ according to Fig 19 (b), which contains two straight lines: $\theta_x = 0$ and $\theta_y = 0$ in the $\theta_x\theta_y$ plane.

The singular posture of $1(R_{eqv1}RPS) - 2(R_{eqv2}PS)$ configuration is the singular surface concentrated near the plane $\theta_z = 0$ as shown in Fig. 19, and the singular curved surface divides the workspace into two parts.

The constraint singularity positions of $3 - R_{eqv2}PS$ configuration are all located are located at both ends of the z -axis in the workspace as shown in Fig. 20, so there remain an entire accessible workspace after eliminating singularity when the mechanism is performing a task.

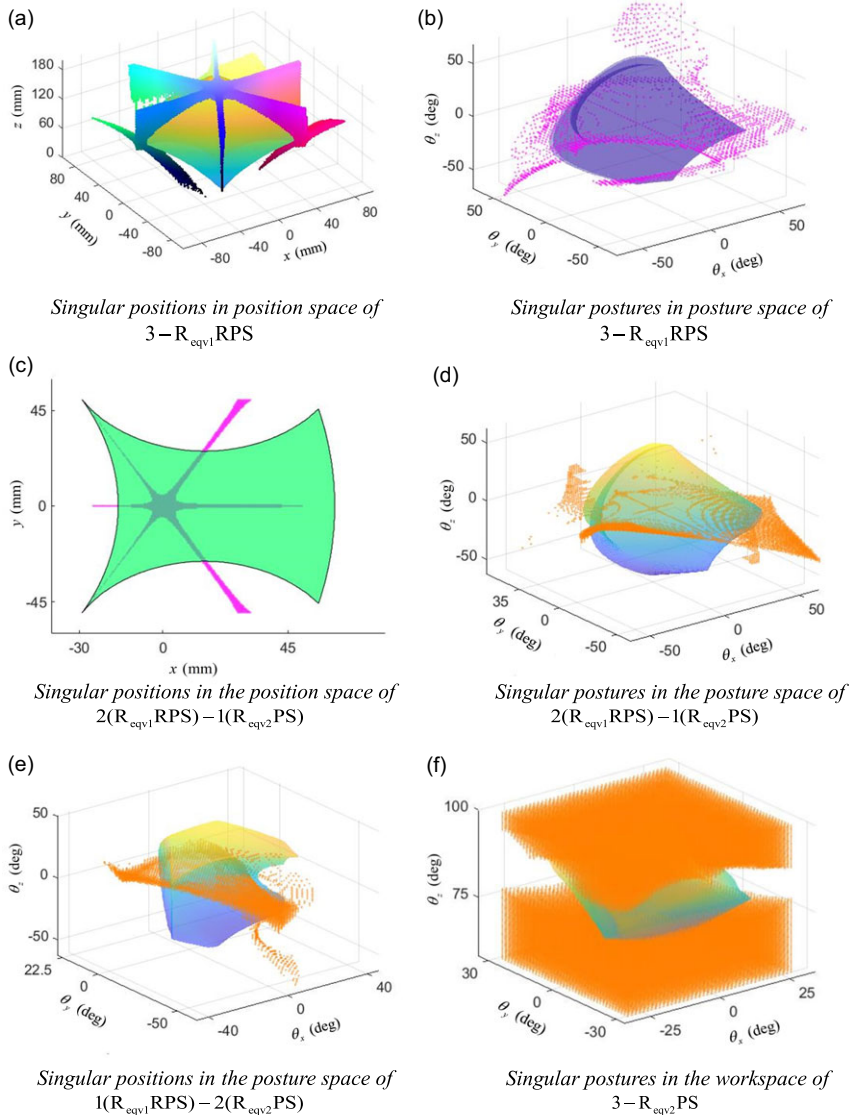


Figure 21. Singularity of the RPM with different configurations in its reachable workspace.

3.4. Discussion

In order to analyze the practicality and application prospects of the four reconfigurable configurations, it is crucial to discuss the distribution of singular configuration points inside and outside the workspace. The constraint singularity in the workspace of the four configurations of the reconfigurable parallel mechanism is shown in Fig. 21, which indicating that the singularities are mainly distributed on special surfaces and planes. As shown in Fig. 21 (a) and (b), the singularity of $3 - R_{eqv1}$ RPS configuration divides the position space into six parts and divides the posture space into upper and lower halves. The branch-chain rotational symmetry of the mechanism at 6-DOF configuration results in a high degree of symmetry in the distribution of singularity points and workspace, which make the mechanism has high potential for practical application. According to Fig. 21 (c), (d), and (e), when locking one or two actuators of the reconfigurable 5R closed-loop linkages, the singularity of RPM does not significantly affect the segmentation of the workspace. However, when locking three actuators of the reconfigurable 5R closed-loop linkages, the singularity of RPM limits its motion to a small range on the z -axis as

shown in Fig. 21 (f). The advantage is that the workspace of the 3-DOF configuration still remains a whole after removing the influence of singular points. This is because after locking the reconfigurable joints in the three branch chains, the mechanism once again has a good geometric relationship with rotational symmetry of the branch chains. In summary, the reconfigurable configurations with 6, 5, and 3 DOF exhibit better kinematic performance than the 4 DOF configuration. Additionally, the mechanism's variable DOF and workspace can meet the practical application of task-oriented parallel mechanisms.

4. Conclusions

This work proposes a reconfigurable joint and designs a reconfigurable parallel mechanism with 4, 5, or 6 DOFs by analyzing the topological changes during the folding process of a single-vertex fivefold origami pattern. The configuration switching of RPM is achieved by utilizing the singular configuration when the origami pattern is fully folded. According to the kinematic analysis of different configurations on the proposed RPM, the following conclusions can be obtained:

1. The spherical 5R mechanism moving in the folding direction of the crease replicates the stabilizing kinematic properties of origami, and the structural constraints and initial position and posture of the reconfigurable parallel mechanism limit the complexity of the kinematic inverse solution, both will promote to reduce the difficulty of controlling the mechanism while performing the desired motion.
2. The proposed new RPM has different DOFs and motion performance after being switched to different configurations, which can realize the multi-purpose of one machine. Even if the DOF of a single direction is limited after configuration switching, the scope of its accessible workspace can still satisfy the general operating requirements.
3. The singularity of the RPM is mainly located in the special planes, after setting the position or posture of the moving platform, the singularity divided the reachable workspace of the mechanism into several parts. Theoretically, the path of the mechanism can be controlled away from the singularity by suitable trajectory planning, which has less influence on the execution of the actual task of the mechanism. Therefore, the mechanism has the potential to adapt to multiple tasks and different working conditions.

Author contributions. Yili Kuang conceived and designed the study. Haibo Qu and Xiao Li provided assistance in singularity analysis. Haibo Qu, Xiaolei Wang, and Sheng Guo Provided suggestions for the writing and polishing of this research.

Financial support. We are grateful for the Supported by the Fundamental Research Funds for the Central Universities (2023JBM013), Hebei Natural Science Foundation (E2022105029), and the National Natural Science Foundation of China (52275004).

Competing interests. The authors declare no competing interests exist.

References

- [1] H. Liu, T. Huang, J. Mei, X. Zhao, D. G. Chetwynd, M. Li and S. Jack Hu, "Kinematic design of a 5-DOF hybrid robot with large workspace/limb-stroke ratio," *J Mech Design* **129**(5), 530–537 (2007).
- [2] P. S. Schenker, P. Pirjanian, J. Balaram, Ali K. S., Trebi-Ollennu A., Huntsberger T. L., Aghazarian H., Kennedy B. A., Baumgartner E. T., Iagnemma K. D., Rzepniewski A., Dubowsky S., Leger P. C., Apostolopoulos D. and McKee G. T., "Reconfigurable Robots for All Terrain Exploration," *In: Proceedings of SPIE - The International Society for Optical Engineering*. 4196, (2000) pp. 454–468.
- [3] V. Zykov, E. Mytilinaios, M. Desnoyer and H. Lipson, "Evolved and designed self-reproducing modular robotics," *IEEE Trans Robot* **23**(2), 308–319 (2007).
- [4] W. Yu, H. Wang and G. Chen, "Design and kinematic analysis of a 3-translational-DOF spatial parallel mechanism based on polyhedral," *Mech Mach Theory* **121**, 92–115 (2018).

- [5] D. Gan, J. S. Dai and D. G. Caldwell, "Constraint-based limb synthesis and mobility-change-aimed mechanism construction," *J Mech Design* **133**(5), 051001 (2011).
- [6] X. Hu and H. Liu, "Design and analysis of full-configuration decoupled actuating reconfigurable parallel spherical joint," *J Mech Sci Technol* **36**(2), 933–945 (2022).
- [7] D. Li, P. Jia, J. Li, D. Zhang and X. Kong, "Constraint and mobility change analysis of rubik's cube-inspired reconfigurable joints and corresponding parallel mechanisms," *Chin J Mech Eng* **33**(1), 81 (2020).
- [8] D. Gan, J. Dias and L. Seneviratne, "Unified kinematics and optimal design of a 3rRPS metamorphic parallel mechanism with a reconfigurable revolute joint," *Mech Mach Theory* **96**, 239–254 (2016).
- [9] W. Ye, X. Chai and K. Zhang, "Kinematic modeling and optimization of a new reconfigurable parallel mechanism," *Mech Mach Theory* **149**, 103850 (2020).
- [10] P. Jia, D. Li, Y. Zhang and C. Yang, "A novel reconfigurable parallel mechanism constructed with spatial metamorphic four-link mechanism," *Proceed Inst Mech Engin, Part C: J Mech Engin Sci* **236**(8), 4120–4132 (2022).
- [11] X. Kong and Y. Jin, "Type synthesis of 3-DOF multi-mode translational/spherical parallel mechanisms with lockable joints," *Mech Mach Theory* **96**, 323–333 (2016).
- [12] G. Coppola, D. Zhang and K. Liu, "A 6-DOF reconfigurable hybrid parallel manipulator," *Robot Com-Integr Manuf* **30**(2), 99–106 (2014).
- [13] J. I. Ibarreche, A. Hernández, V. Petuya and M. Urizar, "A methodology to achieve the set of operation modes of reconfigurable parallel manipulators," *Meccanica* **54**(15), 2507–2520 (2019).
- [14] W. Ye, Y. Fang, S. Guo and Y. Chen, "Two classes of reconfigurable parallel mechanisms constructed with multi-diamond kinematotropic chain," *Proceed Inst Mech Engin, Part C: J Mech Engin Sci* **230**(18), 3319–3330 (2016).
- [15] W. Ye, Y. Fang, K. Zhang and S. Guo, "A new family of reconfigurable parallel mechanisms with diamond kinematotropic chain," *Mech Mach Theory* **74**, 1–9 (2014).
- [16] X. Cui, Y. Sun, Y. Tian, K. Xu and Kuo S., "Mechanical Design and Rolling Locomotion Analyses of a Novel Reconfigurable Mobile Robot Constructed by a Parallel Mechanism," **In: 19th IEEE International Conference on Mechatronics and Automation (IEEE ICMA)**, (2022) pp. 744–748.
- [17] C. Tian, Y. Fang, S. Guo and H. Qu, "A class of reconfigurable parallel mechanisms with five-bar metamorphic linkage," *Proceed Inst Mech Engin, Part C: J Mech Engin Sci* **231**(11), 2089–2099 (2017).
- [18] G. Huang, D. Zhang, S. Guo and H. Qu, "Structural synthesis of a class of reconfigurable parallel manipulators based on over-constrained mechanisms," *Int J Robot Autom* **34**(2), 183–193 (2019).
- [19] J. Wei and J. S. Dai, "Lie group based type synthesis using transformation configuration space for reconfigurable parallel mechanisms with bifurcation between spherical motion and planar motion," *J Mech Design* **142**(6), 063302 (2020).
- [20] J. Wei, C. Qiu and J. S. Dai, "Configuration switch and path selection between schönflies motion and non-schönflies motion based on quotient manifold of novel reconfigurable parallel mechanisms," *Mech Mach Theory* **180**, 105153 (2023).
- [21] C. Tian, D. Zhang, H. Tang and C. Wu, "Structure synthesis of reconfigurable generalized parallel mechanisms with configurable platforms," *Mech Mach Theory* **160**, 104281 (2021).
- [22] X. Kang and J. S. Dai, "Relevance and transferability for parallel mechanisms with reconfigurable platforms," *J Mech Robot* **11**(3), 031012 (2019).
- [23] Y. Xu, Z. Liang and J. Liu, "A new metamorphic parallel leg mechanism with reconfigurable moving platform," *Math Probl Eng* **2020**, 3234969(2020).
- [24] G. Huang, D. Zhang, Q. Zou, W. Ye and L. Kong, "Analysis and design method of a class of reconfigurable parallel mechanisms by using reconfigurable platform," *Mech Mach Theory* **181**, 105215–102023 (2023).
- [25] J. Sun, X. Zhang, G. Wei and J. S. Dai, "Geometry and kinematics for a spherical-base integrated parallel mechanism," *Meccanica* **51**(7), 1607–1621 (2016).
- [26] J. S. Dai, "Survey and Business Case Study of the Dexterous Reconfigurable Assembly and Packaging System (D-RAPS)," **In: Proceedings of the Science and Technology Report. Port Sunlight: Unilever Research: PS960321**, (1996).
- [27] J. S. J. Dai and R. J., "Mobility in Metamorphic Mechanisms of Foldable/Erectable Kinds," **In: Proceedings of 25th ASME Biennial Mechanisms Conference**, (1998).
- [28] H. Fang, Y. Fang and K. Zhang, "Kinematics and workspace analysis of a novel 3-DOF parallel manipulator with virtual symmetric plane," *Proceed Inst Mech Engin Part C J Mech Engin Sci* **227**(3), 620–629 (2013).
- [29] R. Wang, Y. Song and J. S. Dai, "Reconfigurability of the origami-inspired integrated 8R kinematotropic metamorphic mechanism and its evolved 6R and 4R mechanisms," *Mech Mach Theory* **161**, 104245 (2021).
- [30] K. Zhang and C. Liu, "Design and analysis of a novel reconfigurable parallel manipulator with Kirigami-inspired Bennett Plano-spherical linkages and angular pouch motors," *J Mech Rob* **13**(4), 040911 (2021).
- [31] R. L. P. Barreto, F. V. Morlin, M. B. de Souza, A. P. Carboni and D. Martins, "Multiloop origami-inspired spherical mechanisms," *Mech Mach Theory* **155**(1), 104063 (2021).
- [32] Y. Chen, R. Peng and Z. You, "Origami of thick panels," *Science* **349**(6246), 396–400 (2015).
- [33] S.-M. Belcastro and T. C. Hull, "Modelling the folding of paper into three dimensions using affine transformations," *Line Algeb Appl* **348**(1-3), 273–282 (2002).
- [34] L. Zimmermann, K. Shea and T. Stanković, "Conditions for rigid and flat foldability of degree- n vertices in origami," *J Mech Rob* **12**(1), 1–26 (2019).
- [35] X. Wang, H. Qu and S. Guo, "Tristable property and the high stiffness analysis of Kresling pattern origami," *Int J Mech Sci* **256**, 108515 (2023).

[36] X. Wang, H. Qu, X. Li, Y. Kuang, H. Wang and Guo S., “Multi-triangles cylindrical origami and inspired metamaterials with tunable stiffness and stretchable robotic arm,” *PNAS Nexus* **2**(4), pgad098 (2023).

[37] Y. Chen, W. Lv, R. Peng and G. Wei, “Mobile assemblies of four-spherical-4R-integrated linkages and the associated four-crease-integrated rigid origami patterns,” *Mech Mach Theory* **142**, 103613 (2019).

[38] H. Yu, Z. Guo and J. Wang, “A method of calculating the degree of freedom of foldable plate rigid origami with adjacency matrix,” *Adv Mech Eng* **10**(6), 168781401877969 (2018).

[39] J. J. Cervantes-Sánchez, J. C. Hernández-Rodríguez and E. J. González-Galván, “On the 5R spherical, symmetric manipulator: Workspace and singularity characterization,” *Mech Mach Theory* **39**(4), 409–429 (2004).

[40] C. Zhang, Y. Wan, D. Zhang and Q. Ma, “A new mathematical method to study the singularity of 3-RSR multimode mobile parallel mechanism,” *Mathe Probl Engin* **2019**, 1327167 (2019).

[41] M. Özdemir, “Singularity robust balancing of parallel manipulators following inconsistent trajectories,” *Robotica* **34**(9), 2027–2038 (2016). doi: [10.1017/S0263574714002719](https://doi.org/10.1017/S0263574714002719).

[42] W. Bu, “Closeness to singularities of robotic manipulators measured by characteristic angles,” *Robotica* **34**(9), 2105–2115 (2016). doi: [10.1017/S0263574714002823](https://doi.org/10.1017/S0263574714002823).

[43] S. Zarkandi, “A new geometric method for singularity analysis of spherical mechanisms,” *Robotica* **29**(7), 1083–1092 (2011). doi: [10.1017/S0263574711000385](https://doi.org/10.1017/S0263574711000385).

[44] M. Gallant and C. Gosselin, “Singularities of a planar 3-RPR parallel manipulator with joint clearance,” *Robotica* **36**(7), 1098–1109 (2018). doi: [10.1017/S0263574718000279](https://doi.org/10.1017/S0263574718000279).

Appendix

$$l_1 = r_1 + x - r_2 c\theta_y c\theta_z, m_1 = y - r_2 c\theta_y s\theta_z, n_1 = z + r_2 s\theta_y.$$

$$l_2 = \left(2x - r_1 + r_2 c\theta_y c\theta_z + \sqrt{3}r_2 (c\theta_x s\theta_z - c\theta_z s\theta_x s\theta_y) \right) / 2,$$

$$m_2 = \left(2y + \sqrt{3}r_1 + r_2 c\theta_y s\theta_z - \sqrt{3}r_2 (c\theta_x c\theta_z + s\theta_x s\theta_y s\theta_z) \right) / 2, n_2 = z - r_2 \left(\sqrt{3}c\theta_y s\theta_x + s\theta_y \right) / 2.,$$

$$l_3 = \left(2x - r_1 + r_2 c\theta_y c\theta_z + \sqrt{3}r_2 (c\theta_z s\theta_x s\theta_y - c\theta_x s\theta_z) \right) / 2,$$

$$m_3 = \left(2y - \sqrt{3}r_1 + r_2 c\theta_y s\theta_z + \sqrt{3}r_2 (c\theta_x c\theta_z + s\theta_x s\theta_y s\theta_z) \right) / 2, n_3 = z + r_2 \left(\sqrt{3}c\theta_y s\theta_x - s\theta_y \right) / 2.$$

Table AI. Values of actuation Jacobian matrix J_q in different configurations of RPM

RPM configuration	$\begin{pmatrix} Q_{11} & Q_{12} \\ Q_{21} & Q_{22} \end{pmatrix}$	$\begin{pmatrix} Q_{33} & Q_{34} \\ Q_{43} & Q_{44} \end{pmatrix}$	$\begin{pmatrix} Q_{55} & Q_{56} \\ Q_{65} & Q_{66} \end{pmatrix}$
3 – R _{eqv1} RPS	$\begin{pmatrix} \hat{\$}_{r11}^T & \hat{\$}_{12} & \hat{\$}_{r11}^T & \hat{\$}_{13} \\ \hat{\$}_{r12}^T & \hat{\$}_{12} & \hat{\$}_{r12}^T & \hat{\$}_{13} \end{pmatrix}$	$\begin{pmatrix} \hat{\$}_{r21}^T & \hat{\$}_{22} & \hat{\$}_{r21}^T & \hat{\$}_{23} \\ \hat{\$}_{r22}^T & \hat{\$}_{22} & \hat{\$}_{r22}^T & \hat{\$}_{23} \end{pmatrix}$	$\begin{pmatrix} \hat{\$}_{r31}^T & \hat{\$}_{32} & \hat{\$}_{r31}^T & \hat{\$}_{33} \\ \hat{\$}_{r32}^T & \hat{\$}_{32} & \hat{\$}_{r32}^T & \hat{\$}_{33} \end{pmatrix}$
2(R _{eqv1} RPS) – 1(R _{eqv2} PS)	$\begin{pmatrix} 0 & 0 \\ 0 & \hat{\$}_{r13}^T \hat{\$}_{13} \end{pmatrix}$	$\begin{pmatrix} \hat{\$}_{r21}^T & \hat{\$}_{22} & \hat{\$}_{r21}^T & \hat{\$}_{23} \\ \hat{\$}_{r22}^T & \hat{\$}_{22} & \hat{\$}_{r22}^T & \hat{\$}_{23} \end{pmatrix}$	$\begin{pmatrix} \hat{\$}_{r31}^T & \hat{\$}_{32} & \hat{\$}_{r31}^T & \hat{\$}_{33} \\ \hat{\$}_{r32}^T & \hat{\$}_{32} & \hat{\$}_{r32}^T & \hat{\$}_{33} \end{pmatrix}$
1(R _{eqv1} RPS) – 2(R _{eqv2} PS)	$\begin{pmatrix} \hat{\$}_{r11}^T & \hat{\$}_{12} & \hat{\$}_{r11}^T & \hat{\$}_{13} \\ \hat{\$}_{r12}^T & \hat{\$}_{12} & \hat{\$}_{r12}^T & \hat{\$}_{13} \end{pmatrix}$	$\begin{pmatrix} 0 & 0 \\ 0 & \hat{\$}_{r23}^T \hat{\$}_{23} \end{pmatrix}$	$\begin{pmatrix} 0 & 0 \\ 0 & \hat{\$}_{r33}^T \hat{\$}_{33} \end{pmatrix}$
3 – R _{eqv2} PS	$\begin{pmatrix} 0 & 0 \\ 0 & \hat{\$}_{r13}^T \hat{\$}_{13} \end{pmatrix}$	$\begin{pmatrix} 0 & 0 \\ 0 & \hat{\$}_{r23}^T \hat{\$}_{23} \end{pmatrix}$	$\begin{pmatrix} 0 & 0 \\ 0 & \hat{\$}_{r33}^T \hat{\$}_{33} \end{pmatrix}$

Require: $r_1 = 180\text{mm}$, $r_2 = 60\text{mm}$, $x = y = 0$, $z = 90\text{mm}$

Input: range of θ_x , θ_y and θ_z

Output: reachable workspace

```

01: for ( $\theta_x = -1.1$ ,  $\theta_x \leq 1.1$ ,  $\theta_x = \theta_x + 0.01$ )
02:   for ( $\theta_y = -1.1$ ,  $\theta_y \leq 1.1$ ,  $\theta_y = \theta_y + 0.01$ )
03:     for ( $\theta_z = -1.1$ ,  $\theta_z \leq 1.1$ ,  $\theta_z = \theta_z + 0.01$ )
04:       solve  $d_i(i=1, 2, 3)$  according to inverse kinematics equation of RPM
05:       if ( $120 \leq d_i(i=1, 2, 3) \leq 210$ )
06:         solve  $\theta_{4i}(i=1, 2, 3)$  according to inverse kinematics equation of Spherical 5R mechanism
07:         if ( $-\pi \leq \theta_{4i}(i=1, 2, 3) \leq 0$ )
08:           solve  $\psi_i(i=1, 2, 3)$  according to equation (13)
09:           if ( $0 \leq \psi_i(i=1, 2, 3) \leq \pi / 3$ )
10:             record [ $\theta_x, \theta_y, \theta_z$ ]
11:           else
12:             continue
13:           end
14:         else
15:           continue
16:         end
17:       else
18:         continue
19:       end
20:     end
21:   end
22: end
23:  $k = \text{boundary}[\theta_x, \theta_y, \theta_z]$ 
24:  $\text{trimesh}(k)$ 

```

Figure A1. Numerical algorithm to solve the 3 – R_{eqv1} RPS configuration’s workspace.

Require: $r_1 = 180\text{mm}$, $r_2 = 60\text{mm}$, $\theta_x = \theta_y = \theta_z = 0$

Input: range of x , y and z

Output: singular position

```

01: for (x = -50, x ≤ 50, x = x + 1)
02:   for (y = -50, y ≤ 50, y = y + 1)
03:     for (z = 60, z ≤ 170, z = z + 1)
04:       solve  $\hat{\mathbf{S}}_{i1}$  and  $\hat{\mathbf{S}}_{i2}$  ( $i=1, 2, 3$ ) according to DOF of spherical 5R mechanism
05:       solve  $J_x$  and  $J_q$  according to Table 2 and Table 3
06:       if ( $|J_x| \leq 0.0001$  ||  $|J_q| \leq 0.0001$ )
07:         record [x, y, z]
08:       else
09:         continue
10:       end
11:     end
12:   end
13: end
14: scatter 3([x, y, z])

```

Figure A2. Numerical algorithm for solving Jacobian matrix and singularity of 3 – R_{eqv1}RPS configurations.